CHEMISTRY

In situ imaging of the three-dimensional shape of soft responsive particles at fluid interfaces by atomic force microscopy

Jacopo Vialetto*†, Shivaprakash N. Ramakrishna*†, Lucio Isa*

The reconfiguration of individual soft and deformable particles upon adsorption at a fluid interface underpins many aspects of their dynamics and interactions, ultimately regulating the properties of monolayers of relevance for applications. In this work, we demonstrate that atomic force microscopy can be used for the in situ reconstruction of the three-dimensional conformation of model poly(*N*-isopropylacrylamide) microgels adsorbed at an oil-water interface. We image the particle topography from both sides of the interface to characterize its in-plane deformation and to visualize the occurrence of asymmetric swelling in the two fluids. In addition, the technique enables investigating different fluid phases and particle architectures, as well as studying the effect of temperature variations on particle conformation in situ. We envisage that these results open up an exciting range of possibilities to provide microscopic insights into the single-particle behavior of soft objects at fluid interfaces and into the resulting macroscopic material properties.

INTRODUCTION

The confinement of colloidal particles at fluid interfaces holds the key for a broad range of phenomena with applied and fundamental relevance alike, including the stabilization of emulsions and foams (*1*, *2*), the encapsulation and manipulation of liquids (*3*, *4*), and the creation of model two-dimensional (2D) materials (*5*–*9*). In the case of hard, mechanically rigid particles of a given shape, all aspects of their adsorption/desorption, dynamics, and interactions with and at the interface are influenced by a single parameter, the particle contact angle θ, which defines the position of the particle with respect to the interface plane (*10*). Because of its fundamental importance, many techniques have been developed to measure θ (*11*, *12*). However, if the particle is deformable, it can reconfigure upon adsorption under the action of interfacial tension and because of exposure to different solvents (*13*–*15*). Conformational changes and anisotropic deformations relative to the bulk imply that particle properties at the interface can no longer be ascribed to a single parameter and that the notion of a contact angle may no longer be well defined. This more complex response is closely connected to the emergence of additional properties and functionalities, which make soft particles at fluid interfaces highly interesting in formulations, as platforms for materials fabrication and for more fundamental understanding on the 2D phase behavior of compressible objects (*16*, *17*). Consequently, new experimental approaches are required to characterize the 3D shape of soft particles adsorbed at fluid interfaces and infer how this affects their adsorption and desorption, dynamics, and interactions.

Among a broad class of colloidal-scale objects, microgels, i.e., cross-linked polymer particles swollen by the solvent in which they are dispersed, have emerged as a powerful and versatile system. The ease and multiplicity of synthetic strategies to obtain microgels with different internal architectures and polymer compositions (*18*) makes them ideal model systems to elucidate how these parameters affect the adsorption and organization of soft objects at fluid interfaces (*17*). This has allowed their use as synthetic counterparts to proteins and biopolymeric colloids (*19*) and as promising elements for the realization of complex 2D materials (*20*, *21*). Moreover, the incorporation of stimulus-responsive (e.g., temperature, pH, and light) polymers identifies microgels as key elements in smart formulations (*22*). However, as a consequence of their relatively small size and low refractive index mismatch with the solvents, accessing detailed microscopic information on their conformation at the interface remains a daunting task.

Most characterization techniques with single-particle resolution either rely on ex situ investigations, i.e., after transferring the particles from the interface onto a solid support, or give incomplete data, e.g., can only visualize the particle shape with insufficient resolution or have access to one side of the interface only. In particular, in situ techniques based on electron microscopy, such as cryo–scanning electron microscopy (cryo-SEM) (*23*) and freeze-fracture shadow-casting (FreSCa) cryo-SEM (*24*, *25*), or transmission x-ray microscopy (*26*), require fast freezing of the samples and cannot be used to probe the particle response to stimuli in ambient conditions. Moreover, the first two only expose one side of the microgels at the interface and cannot provide real 3D reconstructions. Optical microscopy, including confocal microscopy, requires the use of fluorescent markers and, in any case, does not provide sufficiently high spatial resolution (*23*, *27*–*29*). Conversely, complementary approaches for in situ characterization, such as ellipsometry (*30*) or neutron reflectivity (*31*), provide accurate information on the thickness of adsorbed microgel layers but rely on strong assumptions to extract single-particle conformation. Last, even if deposition and ex situ analysis have been extremely valuable tools for characterizing both the single-particle properties (*25*, *32*–*35*) and the microstructure of the resulting monolayers (*21*, *36*), they have some limitations. The presence of specific interactions between particles and the substrate used may affect the transfer of the microgels and their resulting conformation (*37*). Moreover, the technique can only resolve a 2D projection of the polymer

Laboratory for Soft Materials and Interfaces, Department of Materials, ETH Zürich, Vladimir-Prelog-Weg 5, 8093 Zürich, Switzerland.
*Corresponding author. Email: jacopo.vialetto@mat.ethz.ch (J.V.); shivaprakash.ramakrishna@mat.ethz.ch (S.N.R.); lucio.isa@mat.ethz.ch (L.I.)
†These authors contributed equally to this work.

density distribution across the interface for a particle in dry state and does not give direct access to its 3D conformation at the interface.

In this work, we propose an alternative approach that enables imaging the full 3D shape of soft particles adsorbed at oil-water interfaces at high resolution, using poly(*N*-isopropylacrylamide) (pNIPAM) microgels as model systems, by using in situ atomic force microscopy (AFM).

In situ AFM imaging at fluid interfaces has been previously applied to closely packed nanoparticle monolayers (*38*–*40*) and polymeric films (*41*, *42*) to capture their microstructure in real space with exceptionally high lateral and vertical resolution. Here, we greatly extend the applicability of this technique to include the following: (i) the imaging of dilute layers of soft polymeric particles, allowing us to disclose the reconfiguration of the polymer network upon adsorption at the fluid interface at the single-particle level; (ii) complementary imaging from the oil and water phases to obtain a full 3D shape reconstruction with nanometric resolution; and (iii) temperature-resolved imaging to monitor in situ the response of the pNIPAM network on both sides of the interface below and above the volume phase transition temperature (VPTT) of the microgels ($T \approx 32$°C in water). The versatility of the technique also allows investigating other system parameters, e.g., different organic phases, unraveling how the conformation of the adsorbed particles adapts to changes in the interfacial tension and in the partial solubility of the polymer in the two fluids. Moreover, by using microgels with different internal architecture (in terms of cross-linker content and distribution), we demonstrate that particle design directly affects their conformation at the interface and is thus a crucial parameter influencing the structural and mechanical properties of microgel monolayers.

RESULTS

3D AFM imaging of isolated particles

We begin by describing the experimental setup and the capabilities of the method. Figure 1 schematically illustrates the measurement conditions used for AFM imaging at a liquid-liquid interface. In particular, we use two configurations to image adsorbed particles from both sides of the fluid interface. In a first set of experiments, a dilute aqueous microgel suspension is confined within a thin ring made of ultraviolet light (UV)–curable glue on a silicon wafer (fig. S1). Subsequently, the cell containing the silicon wafer is filled with hexadecane to form the fluid interface to which particles spontaneously adsorb by diffusion. After an equilibration time of about 30 min, the AFM tip is approached to the interface from the oil side, and AFM images are acquired by means of PeakForce Tapping mode (Fig. 1A). In a complementary set of experiments, the thin ring on the silicon wafer is instead filled with hexadecane. A drop of an aqueous suspension of the microgels is then placed on top of the ring to form the interface, and the system is left to equilibrate for approximately 5 min, during which particles reach the fluid interface and adsorb there. Subsequently, the cell is filled with water to remove excess particles not yet adsorbed to the fluid interface. After an additional equilibration time of about 30 min, we then approach the interface with the

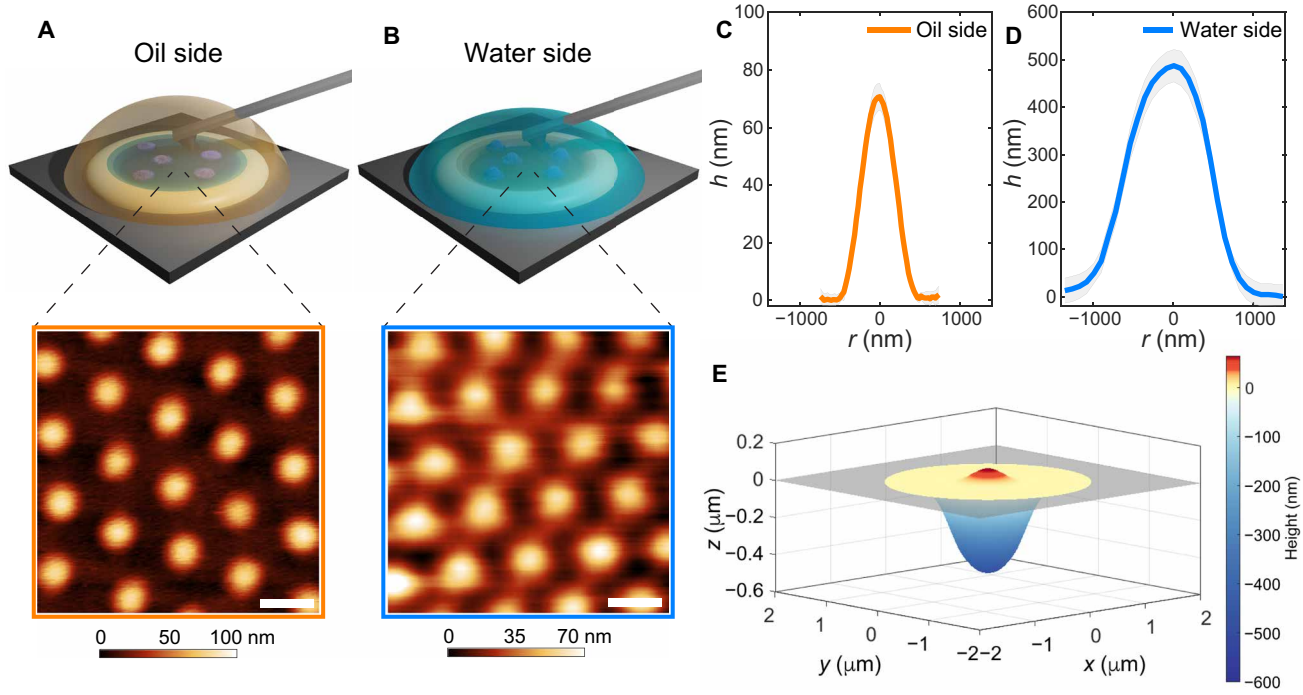

Fig. 1. 3D imaging of microgels adsorbed at a hexadecane-water interface. (**A**) Top: Sketch of the measurement configuration for AFM imaging at the interface between water (subphase) and hexadecane (top phase). Bottom: AFM height image of a microgel monolayer visualized from the oil side. (**B**) Top: Sketch of the complementary measurement configuration with hexadecane as the subphase and water as the top phase. Bottom: AFM height image of a microgel monolayer visualized from the water side. The color bar indicates height variations relative to the lowest point in the image taken as zero. Scale bars, 1 μm. (**C** and **D**) Mean height profiles of isolated adsorbed microgels imaged from the oil (C) and the water (D) side, respectively (corresponding AFM images in fig. S2). The shaded regions correspond to the SDs of the height profiles calculated on at least 10 particles. (**E**) Reconstructed 3D profile across the interface. The gray rectangle indicates the interface plane.

AFM tip from the water side and acquire PeakForce Tapping mode images (Fig. 1B). Additional details on the PeakForce imaging technique are given in the "Materials and Methods" section.

The combination of these two imaging configurations allows for the in situ capturing of the complex 3D conformation of adsorbed soft particles virtually in the same experimental conditions. Representative AFM images of monolayers of standard pNIPAM microgels [labeled *CC5*, showing the typical core-corona profile in bulk water, with 5 mole percent (mol %) *N*,*N*′-methylenebis(acrylamide) (BIS) cross-linker and hydrodynamic diameter D_h = 1150 ± 27 nm; see Materials and Methods] are reported in Fig. 1A (oil side) and Fig. 1B (water side). The technique nicely captures the ordered hexagonal arrangement of the particles in the monolayer from both fluid phases.

From such images, we can also extract quantitative information on the protrusion profiles of the microgels in both phases and on the polymer distribution within the interface plane. Imaging from hexadecane reveals that the microgel is collapsed and barely protrudes out of the interface, reaching, for these particles, a maximum height of 71 ± 5 nm (Fig. 1C). The thickness of the polymer layer decreases from the center toward the edge of the particle and stretches on the plane of the interface for approximately 500 nm in radius. At larger distances from the particle center, the polymer chains adsorbed on the fluid interface are no longer detectable from the height images, while they may remain visible in the adhesion images (see fig. S3).

The complementary images from the water side show a substantially different height profile, which is strongly influenced by the packing of the microgels. The particle conformation departs from the common "fried egg" morphology (*24*, *25*) in closely packed monolayers (Fig. 1B). The polymer networks of neighboring particles in the water phase come into contact and possibly interpenetrate (as discussed in the next section). Swelling of the portion of the particles in contact with water implies that only height variations relative to the lowest point in the image (i.e., between neighboring particles) can be measured. Capturing the full range of the height profiles for microgels from the water side is possible only by imaging isolated or well-separated particles, where the interface plane is also visible as a reference (fig. S2). In such a case, as for the profiles from the oil side, the polymer content decreases from the center of the particle toward the edge (Fig. 1D). However, the peak height is much greater (490 ± 30 nm), and the in-plane dimensions extend to approximately 2100 ± 250 nm.

Merging these two height profiles allows for a complete 3D reconstruction of the conformation of the microgel adsorbed at an oil-water interface, as reported in Fig. 1E. The resulting profile matches the finding of asymmetric shapes deduced by FreSCa cryo-SEM experiments, numerical simulations, and AFM images of microgels transferred onto a solid substrate (*24*, *25*, *35*). However, our measurements provide a direct, quantitative description, which escaped previous approaches.

Imaging particles in contact

After determining the shape of isolated particles, we now move to investigating the conformation of adsorbed microgels in contact. In Fig. 2 (A and B), we report AFM height images of two neighboring particles from both sides of the interface. The reconstructed profiles (Fig. 2C) show that, at the same center-to-center separation, there is significant overlap between the two polymer networks in the water phase, forming a large contact region below the interface with possible compression and interpenetration of the outer part of the microgels, even in the absence of external compression of the interface. Conversely, from the oil side, the particles only sterically interact through their outermost polymer chains adsorbed onto the plane of the interface. The detected height profiles essentially decay to zero in the contact region, and the presence of interacting

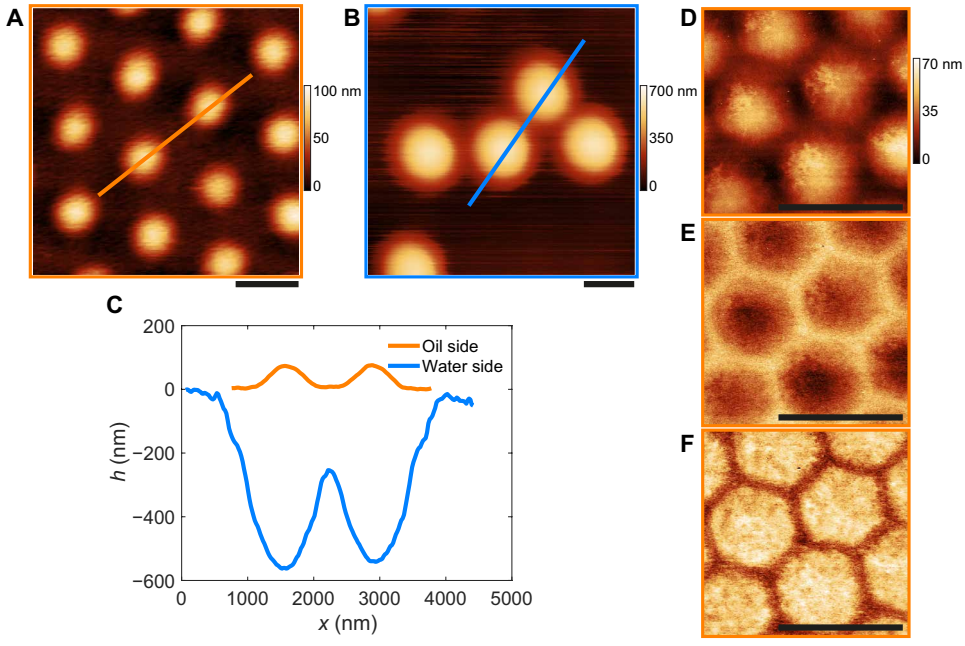

Fig. 2. Conformation of microgels in contact. (**A** and **B**) AFM height images of *CC5* microgels at the hexadecane-water interface visualized from the oil (a) and water (b) side, respectively. (**C**) Height profiles extracted from the images in (A) and (B) along the indicated lines. (**D** to **F**) AFM images of a close-packed monolayer visualized from the oil side. (D) Height, (E) adhesion, and (F) deformation image. Scale bars, 1 μm.

chains is only visible in the adhesion images at this magnification (fig. S3A).

More insights can be gained at a higher magnification as shown in Fig. 2 (D to F). The close-up view of a compact monolayer imaged from the oil side illustrates that high-resolution height images (e.g., as in Fig. 2D) nicely capture the collapsed chains on the surface of the microgels exposed to hexadecane, which aggregate forming globules and bundles onto the particle core, similar to the conformation of collapsed pNIPAM chains measured at high temperature in aqueous conditions on solid supports (*43*). The image also shows that the polymer corona appears to be preferentially localized in the contact regions, forming "polymer bridges." Even if the extent of interpenetration between the coronae of neighboring particles is not directly measurable from the images, examining the adhesion (Fig. 2E) and deformation (Fig. 2F) channels obtained from PeakForce Tapping shows that the particles deform and compress into a closely packed honeycomb contact network (see Materials and Methods for additional information).

These results undoubtedly indicate that the interactions among adsorbed microgels occur both on the plane of the interface, through the adsorbed and stretched polymer coronas, and in the good solvent, where the peripheries of the particles overlap.

Effect of the oil phase

The findings reported above are typical for the case of conventional core-corona microgels exposed to a nonpolar oil with high interfacial tension and where pNIPAM is poorly soluble. Our approach nonetheless enables us to probe the influence of both polymer solubility and interfacial tension on the 3D conformation of the adsorbed microgels by imaging through different oils. In particular, we expect the interfacial tension (γ) to dictate the microgel deformation within the interface plane and to define how the polymer network rearranges upon lateral compression (*44*). To examine markedly different cases, we replaced hexadecane by 1-decanol, therefore switching γ values from $\simeq$50 mN m^{-1} for the hexadecane-water system to $\simeq$9 mN m^{-1} for the 1-decanol–water system. In addition to the drop in interfacial tension, pNIPAM is soluble in fatty alcohols, and consequently, the microgels are expected to swell both in the water and in the oil phase (*28*, *45*).

This hypothesis is confirmed by the in situ AFM height images, reported in Fig. 3 (A and B), and by the corresponding height profiles (Fig. 3C). For a direct comparison, the profiles of the same particles at a hexadecane-water interface are also shown in Fig. 3C (gray dashed and dash-dotted lines). The particles at the 1-decanol–water interface show a similar degree of swelling on both sides of the interface, resulting in an almost symmetrical shape (see also the reconstructed 3D profile in Fig. 3D), which is qualitatively different from the highly asymmetric 3D conformation of the same particles at the hexadecane-water interface. Our imaging enables the quantification of the position of the particle relative to the interface plane, measured as the height ratio h_w/h_o, where h_w and h_o are the maximum height of the particle in water and oil, respectively. The more homogeneous swelling at the 1-decanol–water interface gives h_w/h_o = 0.89 ± 0.04, as opposed to the highly asymmetric conformation of the microgels at the hexadecane-water interface, for which h_w/h_o = 6.9 ± 0.9. This quantification clearly evidences the effect of the solubility in the organic phase on the rearrangement of soft polymeric particles.

Moreover, the reduced value of the interfacial tension leads to a lower deformation within the interface plane, with an interfacial

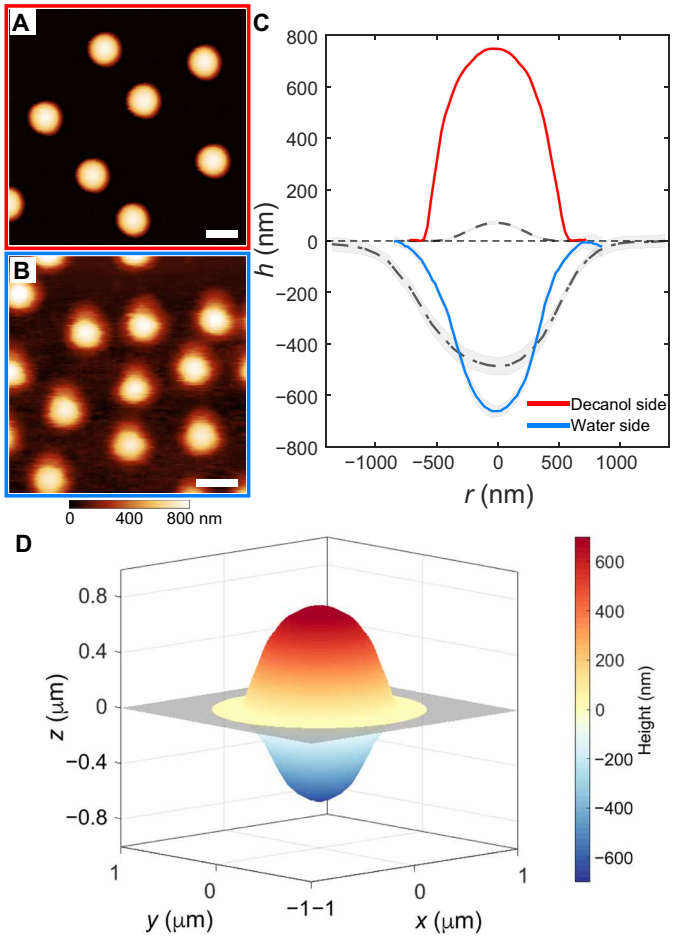

Fig. 3. Influence of the organic phase on the 3D conformation of adsorbed microgels. (**A** and **B**) AFM height images of *CC5* microgels adsorbed at the 1-decanol–water interface, imaged from the 1-decanol (A) and water (B) side, respectively. Scale bars, 1 μm. (**C**) Averaged height profiles of the microgels at the 1-decanol–water interface. The gray dashed and dash-dotted lines represent profiles of the same microgels at the hexadecane-water interface, from the hexadecane and water side, respectively. (**D**) Reconstructed 3D profile across the interface. The gray rectangle indicates the interface plane.

diameter (measured from the water side) of $D_i \simeq$ 1520 nm at the 1-decanol–water interface relative to a value of 2100 nm for the hexadecane-water system. The particle diameter at the interface (D_i) can be used to quantify the stretching ratio of the particles at the interface with respect to their spherical shape in bulk aqueous conditions, defined as D_i/D_h, where D_h is the hydrodynamic diameter measured by dynamic light scattering (DLS). The calculated stretching ratio decreases from 1.8 ± 0.3 to 1.3 ± 0.2, from hexadecane to 1-decanol, indicating the lower degree of deformation at the 1-decanol–water interface. The deviation from a spherical shape is also primarily concentrated in proximity of the interface plane (Fig. 3D), similar to the prediction for neutrally wetting soft spheres (*13*, *15*). We remark that the conformation of a soft particle at a fluid interface is the result of a complex combination of parameters, including γ, the polymer solubility in the two phases, and the particle architecture. Therefore, the position of the geometrical particle center relative to the interface extracted from the 3D reconstruction does not provide direct

information on its affinity for the fluid interface, as it is instead the case for mechanically rigid particles, where there is a clear relationship between particle position, and thus contact angle, and the particle's surface activity. Indeed, in the case of microgels, strong affinity has been reported toward interfaces formed between water and oils of different polarity (*28*, *45*, *46*).

Notably, when imaging denser monolayers, we observe that closely packed hexagonal microgel assemblies can also be obtained at the 1-decanol–water interface (fig. S4). The high swelling on both sides and the limited in-plane deformation prevent accessing the conformation of the polymer corona at the interface, and the particles appear to retain an isotropic shape without rearranging into facets, as it was evidenced at the hexadecane-water interface by imaging the collapsed particles through the oil phase. For this case of symmetrical high swelling, the description of the shape of the microgels at the interface as "fried eggs" is no longer applicable.

Effect of the particle architecture

So far, we have examined only one particle type. However, as previously hinted, the complex 3D conformation of a soft particle adsorbed at the fluid interface is intimately related with the internal architecture of its polymer network, i.e., resulting from the synthesis protocols used (*35*). In Fig. 4, we report a detailed quantification of the profiles of three different microgels adsorbed at the hexadecane-water interface, as a function of their internal polymer density profiles in bulk as measured by static light scattering (SLS) (Fig. 4, A to C; see Materials and Methods). Microgels *CC5* and *CC1* have the typical core-corona profile in water at 25°C, with a denser core and a decrease in polymer content toward the periphery of the particles (*47*, *48*). They differ by the cross-linking content, which is 5 and 1 mol % BIS for *CC5* and *CC1*, respectively, allowing us to investigate the effect of the particle internal elasticity on the network deformation upon interfacial adsorption. Microgel *INV* is instead obtained via a two-step synthesis process (see Materials and Methods), which confers an "inverse" polymer density profile, with a less-dense core and a more cross-linked shell. It is therefore characterized by a qualitatively different density profile than that of *CC5* and *CC1*.

We first describe our observations concerning the shape the particles assume at the fluid interface. We then characterize their full 3D conformation after adsorption by the height (h_w/h_o) and stretching (D_i/D_h) ratios.

The two core-corona microgels have a similar 3D profile after adsorption to the fluid interface (Fig. 4, D and E), with the denser core that protrudes more into the water phase and with a polymer content that continuously decreases toward the particle periphery. The microgel *INV* is, instead, characterized by a much flatter profile on the oil side, with an almost constant thickness up to the visible particle periphery (Fig. 4F). Its conformation in the water phase resembles that of *CC5* and *CC1*, but with quantitative differences, as detailed below. The height ratio increases from 6.9 ± 0.9 for *CC5* to 13.8 ± 1.6 and 33 ± 8 for *CC1* and *INV*, respectively. In the case of more cross-linked particles, their decreased deformability leads to the protrusion of a higher amount of polymer in the organic, immiscible phase. Conversely, for decreasing cross-linking density, and even more so in the absence of a cross-linked core, the particle can stretch further on the interface plane. This characteristic is quantified also by the stretching ratio, which, for microgel *CC5*, is equal to 1.8 ± 0.3, while it reaches 2.0 ± 0.3 for *CC1*, in agreement with

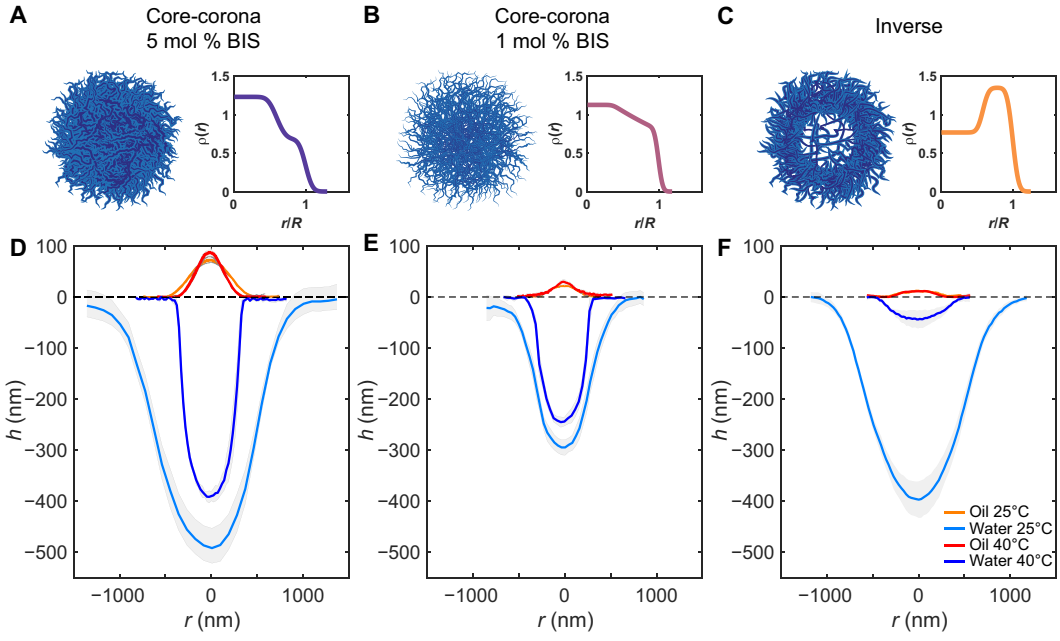

Fig. 4. Conformation of individual microgels at a hexadecane-water interface as a function of internal architecture and temperature. (**A** to **C**) Sketch of the microgels' internal architecture and corresponding polymer density profile [ρ(*r*)] at 25°C plotted as a function of a normalized radial coordinate *r*/*R*, where *R* is the particle radius in bulk, as extracted from fitting of the SLS form factors (see Materials and Methods). (**D** to **F**) Height profiles from AFM images taken from the oil (orange and red curves for profiles at 25° and 40°C, respectively) and water side (light and dark blue curves for profiles at 25° and 40°C, respectively). The shaded regions correspond to the SDs of the height profiles calculated on at least 10 particles. The dotted line indicates the interface plane. The corresponding AFM images are in figs. S2, S5, and S6. (A and D) Core-corona microgel with 5 mol % BIS. (B and E) Core-corona microgel with 1 mol % BIS. (C and F) Microgel with an inverse profile, ultralow cross-linked core, and 5 mol % BIS in the shell.

previous studies reporting an increase in the particle elongation on the interface plane for less cross-linked and, therefore, softer microgels (*25*). We note that we anticipate possible limitations in the detection of the outermost edge of the microgels by the AFM tip in the water phase, as well as at the fluid interface, because of deformation of the solvated chain ends by the approaching AFM tip. Such effect is expected to be more pronounced when particles have a larger amount of loose polymer chains on their surface, as in the case of the less cross-linked *CC1* microgels. Nonetheless, we still observe an increase in the stretching ratio upon decrease of the cross-linking content, albeit of a lower extent than what was observed in literature after transferring microgels onto a solid substrate (*25*). The absence of a cross-linked core allows the *INV* particle to deform even more at the interface to maximize the amount of adsorbed polymer, reaching a value of $D_i/D_h = 2.4 \pm 0.3$, similarly to what has been observed with ultralow cross-linked microgels after transferring onto a solid substrate (*49*).

To conclude, it is instructive to compare in situ AFM imaging with the profiles of the same microgels after transfer on a solid substrate and imaging in the dried state (fig. S7), as this is a commonly used technique to infer information over the microgels' conformation at the fluid interface (*9*, *25*). The "dry" height profiles in fig. S7D show that the overall shape of *CC5* and *CC1* microgels is qualitatively captured, with a Gaussian-like profile that resembles the one imaged from the water side. Conversely, the dry height profile of the *INV* microgel does not match the shape that the particles had at the fluid interface, instead showing a pancake-like conformation (fig. S7, C and D) similar to that assumed by these particles above the VPTT (see following section). When transferring these particles onto a solid substrate, the absence of a cross-linked core causes the entire polymer network to collapse on the interface plane, modifying the conformation assumed at the fluid interface below the VPTT. This emphasizes the importance of an in situ characterization, especially for low cross-linked particles. In addition, the microgels' lateral size, estimated from phase images of deposited microgels, is typically lower than the one obtained directly from in situ AFM at the liquid-liquid interface.

Effect of temperature

pNIPAM microgels are most typically associated with their sharp temperature response in bulk aqueous conditions, and the interplay between interfacial adsorption and temperature has also been extensively explored (*30*, *50*–*52*). However, a direct insight into the conformation changes at the interface for temperatures below and above the solubility transition of pNIPAM is currently lacking.

Our AFM liquid cell allows for accurately controlling the temperature of the sample, enabling us to image the 3D conformation of the microgels across their VPTT. Figure 4 (D to F) reports the height profiles in the water and oil phase for each of the investigated microgels, below and above the VPTT, at 25° and 40°C, respectively. In all cases, at high temperature the particles are stretched out on the interface plane and assume a highly nonspherical shape, with $D_i >> h_w + h_o$, maintaining a core-corona structure. In particular, the profiles on the oil side remain essentially unaltered (orange and red curves): Hexadecane is a bad solvent for pNIPAM irrespective of the solution temperature, and the portion of the microgels exposed to the oil is always collapsed. Conversely, a marked temperature dependence is seen for the portion of the particle in contact with water (light and dark blue curves), with substantial deswelling upon crossing the VPTT.

Because the particles are confined at the interface, the deswelling is anisotropic, different to the isotropic shrinkage of microgels in suspension. We quantify the extent of the interfacial volumetric swelling as a function of temperature in the water phase as the ratio between the volume occupied by the particles in water at 25° and 40°C. For both *CC5* and *CC1*, the volumetric swelling at the interface is much lower than the one in the bulk, reaching 3.0 ± 0.19 and 1.86 ± 0.06 for *CC5* and *CC1*, respectively, while their bulk volumetric swelling is 10.6 ± 0.3 and 15.0 ± 0.3, respectively (see tables S1 and S2). This indicates that, while the particles maintain a thermal responsiveness, the overall degree of deswelling is restrained by the fluid interface. We attribute the apparent decrease in the interfacial volumetric swelling for the less cross-linked microgels to a reduced sensitivity in the detection of the outermost polymer chains of the microgels by the AFM tip in water, which is expected to be particularly relevant for loosely cross-linked chains that are fully solvated at 25°C, as previously mentioned.

We then investigated profiles of particles in contact across the VPTT by comparing AFM images of the same particles at 25° and 40°C from the water (fig. S8) and oil side (fig. S9). Because the distance between the height maxima of two neighboring particles remained approximately constant, we hypothesize that the particles above the VPTT are still in contact via polymer chains that are spread out on the fluid interface plane in a similar way (fig. S8). However, because of the collapse of the polymer shells in the water phase, the particles no longer touch below the interface. On the other hand, the profiles from the hexadecane side remained essentially unaltered (fig. S9). Overall, these results corroborate literature data that reported the presence of a core-corona structure for standard microgels also above the VPTT, as evidenced by ex situ AFM imaging (*52*), and a decrease of the out-of-plane extension of the microgels into the water phase as measured by ellipsometry (*30*, *51*). In addition, they allow quantifying how the contact region between neighboring particles is influenced by the solution temperature.

As previously discussed, the *INV* microgel presents qualitative differences, and its swelling behavior at the interface as a function of temperature emphasizes how the internal architecture controls the particle conformation and response to external stimuli. The presence of an ultralow cross-linked core, which remains highly swollen in water at 25°C, causes a pronounced conformational change when the solution temperature is increased above the VPTT (Fig. 4F). The entire polymer network in the water phase is now collapsed, up to an interfacial volumetric swelling of about 100, leaving only a very thin polymer layer on the fluid surface.

DISCUSSION

The results reported in this work constitute a step forward in accessing the detailed conformation of responsive soft particles adsorbed at fluid interfaces. As it has been demonstrated in the case of bulk microgel systems, novel developments on the visualization of the microgels' internal network are of crucial importance to characterize such complex objects (*53*, *54*), where insight into their 3D shape and deformation enabled an improved understanding of their phase diagram and rheological properties as a function of the effective particle concentration (*55*–*59*). We believe that the imaging technique presented here will, similarly, enable advancing our understanding of the structural and mechanical properties of soft particle monolayers.

As an example, information on the conformation of adsorbed microgels across the VPTT can shed light on the mechanism behind the destabilization of microgel-stabilized emulsions by temperature increase (*50*, *51*). Recently, it has been argued that the collapse of polymer chains onto the microgel core in the water phase plays a central role in causing emulsion destabilization at high temperature because of a decrease of the steric repulsion between two microgel-covered emulsion drops (*52*). The findings we report here enable visualizing and quantifying such an effect, indicating that pronounced deswelling on the water side takes place at high temperatures, suppressing contacts between neighboring particles in the water phase. In addition, in situ AFM imaging shows that the internal architecture of the microgels plays a crucial role in controlling the particle volumetric swelling in the aqueous phase, suggesting that particles with a more loosely cross-linked core will perform as better stabilizers for the production of temperature-sensitive emulsions. Directly verifying how the particle cross-linking density profile unravels at the interface is thus of particular importance in studies on Pickering emulsion stabilization (*23*, *45*).

It is important to remark that the 3D reconstruction of the particle shape enables us to identify the position of the geometrical particle center relative to the interface. However, this does not directly reflect the position of the particle's center of mass, as our volumetric analysis does not provide direct information on the distribution of the polymer mass in the two phases, which depends on the specific solvent uptake in the two fluids. Therefore, it is not possible to relate the position of the microgel's geometrical center to its affinity for the fluid interface, as it would be the case for the definition of the contact angle value for mechanically rigid particles. However, it still provides quantitative information on the microgel's conformation as a function of the organic phase or of temperature. In situ visualization of the microgel's conformation at the 1-decanol–water interface unambiguously shows how the particles deviate from the common fried egg shape when the polymer solubility in the top phase increases and the in-plane force exerted by interfacial tension decreases. Direct imaging illustrates that particle properties can also be tuned by changing the top fluid phase, in addition to modifying microgel architecture during synthesis, and can help explain the stabilization of oil-in-water or water-in-oil emulsions depending on the polarity of the organic phase (*28*).

Similarly, these findings illustrate that reconstructing the full 3D shape of the microgels is important to describe interactions in ordered monolayers, where interparticle contacts can happen both at the interface and through the bulk liquids, therefore opening the way to a more advanced control over the monolayer microstructure and mechanical properties in response to interfacial stresses (*35*). Further experiments in which the profile of adsorbed microgels is captured as a function not only of temperature but also of their packing fraction, will help elucidate how compression and interactions affect their conformation in crowded environments. Overall, we envisage that in situ AFM imaging will greatly enhance the toolbox of available characterization techniques of microgel monolayers, which can now be applied to a multitude of soft particles at interfaces as an exciting way to explore their properties and tackle open questions.

MATERIALS AND METHODS

Reagents

BIS (Fluka, 99.0%), methacrylic acid (MAA; Acros Organics, 99.5%), potassium persulfate (KPS; Sigma-Aldrich, 99.0%), isopropanol (Fisher Chemical, 99.97%), toluene (Fluka Analytical, 99.7%), *n*-hexane (Sigma-Aldrich; high-performance liquid chromatography–grade, 95%), *n*-hexadecane (Acros Organics, 99.0%), and 1-decanol (Sigma-Aldrich, ≥98%) were used without further purification. NIPAM (TCI, 98.0%) was purified by recrystallization in 40/60 (v/v) toluene/hexane.

Microgels synthesis

The microgels used in this study were synthesized by free-radical precipitation polymerization.

Soft microgels—CC1

NIPAM (0.385 g), 5 mol % MAA, and 1 mol % BIS were dissolved in 25 ml of ultrapure water at room temperature. The reaction mixture was then immersed into an oil bath at 80°C and purged with nitrogen for 1 hour. The reaction was started by adding 10 mg of KPS previously dissolved in 1 ml of MQ water and purged with nitrogen. The polymerization was carried out for 6 hours in a sealed flask. Afterward, the colloidal suspension was cleaned by dialysis for a week and eight centrifugation cycles and resuspension of the sedimented particles in ultrapure water.

Stiff microgels—CC5

NIPAM (1 g), 5 mol % MAA, and 5 mol % BIS were dissolved in 50 ml of ultrapure water at room temperature. The reaction mixture was then purged with nitrogen for 1 hour. Afterward, 40 ml of the monomer solution was taken out with a syringe. Ten milliliters of ultrapure water was added to the reaction flask, and the solution was immersed into an oil bath at 80°C and purged with nitrogen for another 30 min. The reaction was started by adding 13 mg of KPS previously dissolved in 1 ml of MQ water and purged with nitrogen. After 1.5 min, the solution turned slightly milky, and feeding of the monomer solution (40 ml at 0.5 ml min^{-1}) to the reaction flask was started. When feeding was terminated, the reaction was immediately quenched by opening the flask to let the air in and placing it in an ice bath. The obtained colloidal suspension was cleaned by dialysis for a week and by eight centrifugation cycles and resuspension of the sedimented particles in ultrapure water.

Inverse microgels—INV

This is a two-step synthesis devised to produce core-shell microgels having an ultralow cross-linked core (*60*) covered by a cross-linked shell. NIPAM (0.5 g) and 5 mol % MAA were dissolved in 50 ml of ultrapure water at room temperature. The reaction mixture was then purged with nitrogen for 1 hour and immersed into an oil bath at 80°C. Fifty milligrams of KPS, previously dissolved in 2 ml of ultrapure water and purged with nitrogen, was added to the flask to start the reaction. Meanwhile, in a separate flask, a second monomer solution was prepared, containing NIPAM (0.5 g), 5 mol % MAA, and 5 mol % BIS dissolved in 40 ml of ultrapure water, purged with nitrogen for 1 hour, and then transferred to a syringe. In addition, 13 mg of KPS was dissolved in 1 ml of ultrapure water and purged with nitrogen. After 1 hour and 30 min since the beginning of the reaction, 13 mg of KPS was added to the reaction flask, immediately followed by the second monomer solution, which was added dropwise at a feeding rate of 0.5 ml min^{-1}. When feeding was terminated, the reaction was immediately quenched by opening the flask to let the air in and placing it in an ice bath. The obtained colloidal suspension was cleaned by dialysis for a week and by eight centrifugation cycles and resuspension of the sedimented particles in ultrapure water.

Methods

DLS and SLS

DLS experiments were performed using a Zetasizer (Malvern, UK). The scattering vector for DLS experiments was $q = 0.026\ nm^{-1}$. The samples were left to equilibrate for 15 min at the required temperature (22° or 40°C) before performing six consecutive measurements. For SLS, a CGS-3 compact goniometer (ALV, Germany) system was used, equipped with a Nd–yttrium-aluminum-garnet laser, $\lambda = 532$ nm, an output power of 50 mW before an optical insulator, and measuring angles from 30° to 150° with 5° or 2° steps. Static scattering form factor analysis was performed using the FitIt! tool developed by Otto Virtanen for MATLAB (*60*). A detailed description of the fitting procedure is reported elsewhere (*35*).

Deposition of isolated microgels from a liquid-liquid interface

Microgels were deposited from a hexane-water interface onto silicon wafers for AFM imaging of isolated dried particles following an already reported procedure (*35*, *44*). Silicon wafers were cut into pieces and cleaned by 15 min of ultrasonication in toluene, isopropanol, acetone, ethanol, and ultrapure water. A piece was then placed inside a Teflon beaker on the arm of a linear motion driver and immersed in water. Successively, a liquid interface was created between water and *n*-hexane. Around 100 μl of the microgel suspension was injected at the interface after appropriate dilution in a 4:1 water:isopropanol solution. After 10 min of equilibration, extraction of the substrate was conducted at a speed of 25 $\mu m\ s^{-1}$ to collect the microgels adsorbed at the liquid interface. Note that given the almost identical solubility parameters for pNIPAM in hexane and hexadecane, as well as their very similar interfacial tensions, we do not expect any conformational difference of the microgels at the two interfaces. Hexane is, however, chosen for the depositions for its low viscosity and high volatility, which minimize distortions during transfer (*61*).

AFM imaging and analysis

Imaging of microgels at the liquid-liquid interface was carried out using a Bruker Dimension Icon AFM. At first, a small well was made by applying a drop of UV curable glue (Norland Optical Adhesive 81) on a piece of silicon wafer (Si-Mat, Landsberg, Germany) using a pipette tip. This well (average depth of 2 to 10 μm) acts as a reservoir for containing the subphase (oil or water). Figure S1 shows an optical profilometer image of such a reservoir on the silicon surface. The wafer was then glued to a bio heater cell (MFP 3D, Asylum Research, Oxford Instrument). Before each AFM experiment, the cell was cleaned with ethanol, and the silicon wafer was plasma cleaned for 10 s using a plasma pen (Piezobrush PZ2, Relyon Plasma GmbH, Germany). For imaging from the oil phase, the reservoir was filled with 5 μl of the microgel suspension in water. After 5 min, the entire cell was filled with the oil (hexadecane or 1-decanol). We then waited for approximately 30 min before imaging to allow for the cell's temperature to equilibrate after turning on the AFM laser and immersing the cantilever and for the cessation of residual convection after fluid injection. After this equilibration time, drift at the interface was greatly reduced, allowing for the stable capturing of high-resolution images. For imaging from the water phase, the reservoir was first filled with oil, and then ~5 μl of the microgel suspension in water was injected on top of the oil. After 5 min, the entire cell was filled with water. The water was exchanged two times to avoid multilayer formation and to remove any excess of microgels floating in the bulk phase. The bio heater cell was placed under the AFM, and the imaging was started after around 30 min to allow for the stabilization of the interface, analogously to the procedure followed in the case of imaging from the oil side.

AFM imaging at the interface was carried out using PeakForce Tapping mode. For the hexadecane-water interface, cantilevers with a nominal spring constant of $\sim 0.12\ N\ m^{-1}$ (PEAKFORCE-HIRS-F-B, Bruker) were chosen for imaging. The tip was approached to the interface by setting a PeakForce setpoint of 100 pN and adjusted slightly along with the feedback gains once the tip was engaged at the interface. The PeakForce during the imaging was varied between 100 and 500 pN with the aim of obtaining images with the highest quality. The imaging at the 1-decanol–water interface was done using much softer cantilevers because of the low interfacial tension (nominal spring constant of $\sim 0.03\ N\ m^{-1}$; CSG01, NT-MDT). The PeakForce setpoint during tip engagement was kept as low as 5 pN and was varied between 5 and 20 pN while imaging to avoid snapping-in of the cantilever into the subphase. The PeakForce amplitude during imaging in the various fluid phases was varied between 100 and 300 nm. The PeakForce frequency was chosen between 1 and 2 kHz and the scanning rate was between 0.2 and 1 Hz. The chemistry of the AFM tips was not controlled, using cantilevers taken directly out of the box and using the same tips multiple times. Static contact angle measurements of a 1-μl water drop deposited on the chip of the untreated AFM tips from the box (either new or after use and rinsing with ethanol) consistently revealed an intermediate hydrophobicity (contact angle of 80° ± 3°).

Along with topographical images, adhesion and deformation images were also captured in PeakForce Tapping mode. However, as the PeakForce setpoint during the imaging was limited to 100 to 500 pN, the force curves are influenced by multiple factors (*62*). As a consequence, it is not possible to infer quantitative information from the deformation and adhesion channels. Specifically, the adhesion signal is directly affected by the tip-sample interactions, which depend on the tip's chemistry, and the deformation signal includes both the mechanical deformation of the polymer owing to indentation with the sharp AFM tip and repulsive interactions between the tip and the sample. Therefore, we make use of the adhesion and deformation channels obtained from the PeakForce Tapping imaging only to highlight aspects of the conformation of adsorbed particles in a way that is otherwise difficult to visualize directly from the height images.

Dry microgels deposited on silicon wafers were imaged in Tapping mode, using cantilevers with ~300 kHz resonance frequency and $\sim 26\ N\ m^{-1}$ spring constant (AC160TS-R3, Olympus Cantilevers, Japan). Height and phase images were recorded at the same time.

All AFM images were first processed with open-source software Gwyddion and successively analyzed with custom MATLAB codes. Imaging from the water side is subjected to more noise with respect to imaging from the oil phase, especially between lines perpendicular to the scanning direction. Therefore, some images, such as the one in Fig. 1B, have been corrected with a correlation-averaging algorithm in the Gwyddion software before further analysis. The following procedure was used to obtain an averaged height profile: For each microgel, horizontal and vertical profiles passing through its center were extracted. Subsequently, an average over at least 10 microgels was obtained by aligning each profile by its center value. To reconstruct the entire profile of a microgel adsorbed at the fluid interface, the profile measured on the water side was inverted to appear below the interface plane. The 3D reconstructions in Figs. 1E and 3D are obtained by rotating the height profiles for $r > 0$ around

the y axis. The volume occupied by the particle in the water phase was calculated as

$$V_{\text{int}} = \pi \int [f(r)]^2 \, dr$$

where $f(r)$ is the radial profile in the water phase at the given temperature.

Profilometry

A 3D optical profilometer (Sensofar PLu Neox, Sensofar-Tech, S.L., Terrassa, Spain) operating in confocal mode with a 5× objective was used to measure the depth of the reservoir made on the silicon wafer.

SUPPLEMENTARY MATERIALS

Supplementary material for this article is available at https://science.org/doi/10.1126/sciadv.abq2019

REFERENCES AND NOTES

1. B. P. Binks, R. Murakami, Phase inversion of particle-stabilized materials from foams to dry water. *Nat. Mater.* **5**, 865–869 (2006).
2. U. T. Gonzenbach, A. R. Studart, E. Tervoort, L. J. Gauckler, Ultrastable particle-stabilized foams. *Angew. Chem. Int. Ed.* **45**, 3526–3530 (2006).
3. M. F. Haase, K. J. Stebe, D. Lee, Continuous fabrication of hierarchical and asymmetric bijel microparticles, fibers, and membranes by solvent transfer-induced phase separation (STRIPS). *Adv. Mater.* **27**, 7065–7071 (2015).
4. M. Anyfantakis, V. S. R. Jampani, R. Kizhakidathazhath, B. P. Binks, J. P. F. Lagerwall, Responsive photonic liquid marbles. *Angew. Chem. Int. Ed.* **59**, 19260–19267 (2020).
5. A. D. Law, D. M. A. Buzza, T. S. Horozov, Two-dimensional colloidal alloys. *Phys. Rev. Lett.* **106**, 128302 (2011).
6. N. C. Keim, P. E. Arratia, Mechanical and microscopic properties of the reversible plastic regime in a 2D jammed material. *Phys. Rev. Lett.* **112**, 028302 (2014).
7. I. Buttinoni, M. Steinacher, H. T. Spanke, J. Pokki, S. Bahmann, B. Nelson, G. Foffi, L. Isa, Colloidal polycrystalline monolayers under oscillatory shear. *Phys. Rev. E* **95**, 012610 (2017).
8. J. Vialetto, S. Rudiuk, M. Morel, D. Baigl, Photothermally reconfigurable colloidal crystals at a fluid interface, a generic approach for optically tunable lattice properties. *J. Am. Chem. Soc.* **143**, 11535–11543 (2021).
9. J. Menath, J. Eatson, R. Brilmayer, A. Andrieu-Brunsen, D. M. A. Buzza, N. Vogel, Defined core–shell particles as the key to complex interfacial selfassembly. *Proc. Natl. Acad. Sci. U.S.A.* **118**, e2113394118 (2021).
10. F. Bresme, M. Oettel, Nanoparticles at fluid interfaces. *J. Phys. Condens. Matter* **19**, 413101 (2007).
11. A. Maestro, E. Guzmán, F. Ortega, R. G. Rubio, Contact angle of micro- and nanoparticles at fluid interfaces. *Curr. Opin. Colloid Interface Sci.* **19**, 355–367 (2014).
12. M. Zanini, L. Isa, Particle contact angles at fluid interfaces: Pushing the boundary beyond hard uniform spherical colloids. *J. Phys. Condens. Matter* **28**, 313002 (2016).
13. R. W. Style, L. Isa, E. R. Dufresne, Adsorption of soft particles at fluid interfaces. *Soft Matter* **11**, 7412–7419 (2015).
14. H. Mehrabian, J. Harting, J. H. Snoeijer, Soft particles at a fluid interface. *Soft Matter* **12**, 1062–1073 (2016).
15. J. Kolker, L. Fischer, A. M. Menzel, H. Löwen, Elastic deformations of spherical core-shell systems under an equatorial load. *J. Elast.* **150**, 77–89 (2022).
16. M. Karg, A. Pich, T. Hellweg, T. Hoare, L. A. Lyon, J. J. Crassous, D. Suzuki, R. A. Gumerov, S. Schneider, I. I. Potemkin, W. Richtering, Nanogels and microgels: From model colloids to applications, recent developments, and future trends. *Langmuir* **35**, 6231–6255 (2019).
17. M. Rey, M. A. Fernandez-Rodriguez, M. Karg, L. Isa, N. Vogel, Poly-N-isopropylacrylamide nanogels and microgels at fluid interfaces. *Acc. Chem. Res.* **53**, 414–424 (2020).
18. F. A. Plamper, W. Richtering, Functional microgels and microgel systems. *Acc. Chem. Res.* **50**, 131–140 (2017).
19. B. S. Murray, Microgels at fluid-fluid interfaces for food and drinks. *Adv. Colloid Interface Sci.* **271**, 101990 (2019).
20. B. M. Rey, R. Elnathan, R. Ditcovski, K. Geisel, M. Zanini, M. A. Fernandez-Rodriguez, V. V. Naik, A. Frutiger, W. Richtering, T. Ellenbogen, N. H. Voelcker, L. Isa, Fully tunable silicon nanowire arrays fabricated by soft nanoparticle templating. *Nano Lett.* **16**, 157–163 (2016).
21. F. Grillo, M. A. Fernandez-Rodriguez, M.-N. Antonopoulou, D. Gerber, L. Isa, Self-templating assembly of soft microparticles into complex tessellations. *Nature* **582**, 219–224 (2020).
22. T. Liu, S. Seiffert, J. Thiele, A. R. Abate, D. A. Weitz, W. Richtering, Non-coalescence of oppositely charged droplets in pH-sensitive emulsions. *Proc. Natl. Acad. Sci. U.S.A.* **109**, 384–389 (2012).
23. M. Destribats, V. Lapeyre, M. Wolfs, E. Sellier, F. Leal-Calderon, V. Ravaine, V. Schmitt, Soft microgels as Pickering emulsion stabilisers: Role of particle deformability. *Soft Matter* **7**, 7689 (2011).
24. K. Geisel, L. Isa, W. Richtering, Unraveling the 3D localization and deformation of responsive microgels at oil/water interfaces: A step forward in understanding soft emulsion stabilizers. *Langmuir* **28**, 15770–15776 (2012).
25. F. Camerin, M. Á. Fernández-Rodríguez, L. Rovigatti, M. N. Antonopoulou, N. Gnan, A. Ninarello, L. Isa, E. Zaccarelli, Microgels adsorbed at liquid–liquid interfaces: A joint numerical and experimental study. *ACS Nano* **13**, 4548–4559 (2019).
26. K. Geisel, K. Henzler, P. Guttmann, W. Richtering, New insight into microgel-stabilized emulsions using transmission X-ray microscopy: Nonuniform deformation and arrangement of microgels at liquid interfaces. *Langmuir* **31**, 83–89 (2015).
27. K. Horigome, D. Suzuki, Drying mechanism of poly(N-isopropylacrylamide) microgel dispersions. *Langmuir* **28**, 12962–12970 (2012).
28. M. Destribats, V. Lapeyre, E. Sellier, F. Leal-Calderon, V. Schmitt, V. Ravaine, Water-in-oil emulsions stabilized by water-dispersible poly(N-isopropylacrylamide) microgels: Understanding anti-finkle behavior. *Langmuir* **27**, 14096–14107 (2011).
29. M.-H. Kwok, T. Ngai, A confocal microscopy study of micron-sized poly(N-isopropylacrylamide) microgel particles at the oil–water interface and anisotopic flattening of highly swollen microgel. *J. Colloid Interface Sci.* **461**, 409–418 (2016).
30. S. Bochenek, A. Scotti, W. Ogieglo, M. Á. Fernández-Rodríguez, M. F. Schulte, R. A. Gumerov, N. V. Bushuev, I. I. Potemkin, M. Wessling, L. Isa, W. Richtering, Effect of the 3D swelling of microgels on their 2D phase behavior at the liquid–liquid interface. *Langmuir* **35**, 16780–16792 (2019).
31. K. Zielińska, R. A. Campbell, A. Zarbakhsh, M. Resmini, Adsorption versus aggregation of NIPAM nanogels: New insight into their behaviour at the air/water interface as a function of concentration. *Phys. Chem. Chem. Phys.* **19**, 17173–17179 (2017).
32. A. Aufderhorst-Roberts, D. Baker, R. J. Foster, O. Cayre, J. Mattsson, S. D. Connell, Nanoscale mechanics of microgel particles. *Nanoscale* **10**, 16050–16061 (2018).
33. S. A. Vasudevan, A. Rauh, M. Kröger, M. Karg, L. Isa, Dynamics and wetting behavior of core–shell soft particles at a fluid–fluid interface. *Langmuir* **34**, 15370–15382 (2018).
34. G. Li, I. Varga, A. Kardos, I. Dobryden, P. M. Claesson, Temperature-dependent nanomechanical properties of adsorbed poly-NIPAm microgel particles immersed in water. *Langmuir* **37**, 1902–1912 (2021).
35. J. Vialetto, F. Camerin, F. Grillo, S. N. Ramakrishna, L. Rovigatti, E. Zaccarelli, L. Isa, Effect of internal architecture on the assembly of soft particles at fluid interfaces. *ACS Nano* **15**, 13105–13117 (2021).
36. M. Rey, M. Á. Fernández-Rodríguez, M. Steinacher, L. Scheidegger, K. Geisel, W. Richtering, T. M. Squires, L. Isa, Isostructural solid–solid phase transition in monolayers of soft core–shell particles at fluid interfaces: Structure and mechanics. *Soft Matter* **12**, 3545–3557 (2016).
37. L. Hoppe Alvarez, A. A. Rudov, R. A. Gumerov, P. Lenssen, U. Simon, I. I. Potemkin, D. Wöll, Controlling microgel deformation via deposition method and surface functionalization of solid supports. *Phys. Chem. Chem. Phys.* **23**, 4927–4934 (2021).
38. L. Costa, G. Li-Destri, N. H. Thomson, O. Konovalov, D. Pontoni, Real space imaging of nanoparticle assembly at liquid–liquid interfaces with nanoscale resolution. *Nano Lett.* **16**, 5463–5468 (2016).
39. Y. Chai, A. Lukito, Y. Jiang, P. D. Ashby, T. P. Russell, Fine-tuning nanoparticle packing at water–oil interfaces using ionic strength. *Nano Lett.* **17**, 6453–6457 (2017).
40. Y. Chai, J. Hasnain, K. Bahl, M. Wong, D. Li, P. Geissler, P. Y. Kim, Y. Jiang, P. Gu, S. Li, D. Lei, B. A. Helms, T. P. Russell, P. D. Ashby, Direct observation of nanoparticle-surfactant assembly and jamming at the water-oil interface. *Sci. Adv.* **6**, eabb8675 (2020).
41. L. Costa, G. Li-Destri, D. Pontoni, O. Konovalov, N. H. Thomson, Liquid-liquid interfacial imaging using atomic force microscopy. *Adv. Mater. Interfaces* **4**, 1700203 (2017).
42. P.-Y. Gu, Y. Chai, H. Hou, G. Xie, Y. Jiang, Q.-F. Xu, F. Liu, P. D. Ashby, J.-M. Lu, T. P. Russell, Stabilizing liquids using interfacial supramolecular polymerization. *Angew. Chem. Int. Ed.* **58**, 12112–12116 (2019).
43. E. M. Benetti, S. Zapotoczny, G. J. Vancso, Tunable thermoresponsive polymeric platforms on gold by "photoiniferter"-based surface grafting. *Adv. Mater.* **19**, 268–271 (2007).
44. J. Vialetto, N. Nussbaum, J. Bergfreund, P. Fischer, L. Isa, Influence of the interfacial tension on the microstructural and mechanical properties of microgels at fluid interfaces. *J. Colloid Interface Sci.* **608**, 2584–2592 (2021).
45. S. Schmidt, T. Liu, S. Rütten, K. H. Phan, M. Möller, W. Richtering, Influence of microgel architecture and oil polarity on stabilization of emulsions by stimuli-sensitive core–shell poly(N-isopropylacrylamide-co-methacrylic acid) microgels: Mickering versus pickering behavior? *Langmuir* **27**, 9801–9806 (2011).
46. N. Nussbaum, J. Bergfreund, J. Vialetto, L. Isa, P. Fischer, Microgels as globular protein model systems. *Colloids Surf. B Biointerfaces* **217**, 112595 (2022).

47. M. Stieger, W. Richtering, J. S. Pedersen, P. Lindner, Small-angle neutron scattering study of structural changes in temperature sensitive microgel colloids. *J. Chem. Phys.* **120**, 6197–6206 (2004).
48. A. Ninarello, J. J. Crassous, D. Paloli, F. Camerin, N. Gnan, L. Rovigatti, P. Schurtenberger, E. Zaccarelli, Modeling microgels with a controlled structure across the volume phase transition. *Macromolecules* **52**, 7584–7592 (2019).
49. A. Scotti, S. Bochenek, M. Brugnoni, M. A. Fernandez-Rodriguez, M. F. Schulte, J. E. Houston, A. P. H. Gelissen, I. I. Potemkin, L. Isa, W. Richtering, Exploring the colloid-to-polymer transition for ultra-low crosslinked microgels from three to two dimensions. *Nat. Commun.* **10**, 1418 (2019).
50. C. Monteux, C. Marlière, P. Paris, N. Pantoustier, N. Sanson, P. Perrin, Poly(N-isopropylacrylamide) microgels at the oil-water interface: Interfacial properties as a function of temperature. *Langmuir* **26**, 13839–13846 (2010).
51. A. Maestro, D. Jones, C. S. de Rojas Candela, E. Guzman, M. H. G. Duits, P. Cicuta, Tuning interfacial properties and processes by controlling the rheology and structure of poly(N-isopropylacrylamide) particles at air/water interfaces. *Langmuir* **34**, 7067–7076 (2018).
52. J. Harrer, M. Rey, S. Ciarella, H. Löwen, L. M. C. Janssen, N. Vogel, Stimuli-responsive behavior of PNiPAm microgels under interfacial confinement. *Langmuir* **35**, 10512–10521 (2019).
53. A. P. H. Gelissen, A. Oppermann, T. Caumanns, P. Hebbeker, S. K. Turnhoff, R. Tiwari, S. Eisold, U. Simon, Y. Lu, J. Mayer, W. Richtering, A. Walther, D. Wöll, 3D structures of responsive nanocompartmentalized microgels. *Nano Lett.* **16**, 7295–7301 (2016).
54. S. Bergmann, O. Wrede, T. Huser, T. Hellweg, Super-resolution optical microscopy resolves network morphology of smart colloidal microgels. *Phys. Chem. Chem. Phys.* **20**, 5074–5083 (2018).
55. D. Paloli, P. S. Mohanty, J. J. Crassous, E. Zaccarelli, P. Schurtenberger, Fluid–solid transitions in soft-repulsive colloids. *Soft Matter* **9**, 3000 (2013).
56. Y. Peng, F. Wang, Z. Wang, A. M. Alsayed, Z. Zhang, A. G. Yodh, Y. Han, Two-step nucleation mechanism in solid–solid phase transitions. *Nat. Mater.* **14**, 101–108 (2015).
57. G. M. Conley, P. Aebischer, S. Nöjd, P. Schurtenberger, F. Scheffold, Jamming and overpacking fuzzy microgels: Deformation, interpenetration, and compression. *Sci. Adv.* **3**, e1700969 (2017).
58. M. J. Bergman, N. Gnan, M. Obiols-Rabasa, J. M. Meijer, L. Rovigatti, E. Zaccarelli, P. Schurtenberger, A new look at effective interactions between microgel particles. *Nat. Commun.* **9**, 5039 (2018).
59. A. Scotti, J. E. Houston, M. Brugnoni, M. M. Schmidt, M. F. Schulte, S. Bochenek, R. Schweins, A. Feoktystov, A. Radulescu, W. Richtering, Phase behavior of ultrasoft spheres show stable bcc lattices. *Phys. Rev. E* **102**, 052602 (2020).
60. O. L. J. Virtanen, A. Mourran, P. T. Pinard, W. Richtering, Persulfate initiated ultra-low cross-linked poly(N-isopropylacrylamide) microgels possess an unusual inverted crosslinking structure. *Soft Matter* **12**, 3919–3928 (2016).
61. L. Isa, K. Kumar, M. Müller, J. Grolig, M. Textor, E. Reimhult, Particle lithography from colloidal self-assembly at liquid-liquid interfaces. *ACS Nano* **4**, 5665–5670 (2010).
62. I. Medalsy, U. Hensen, D. J. Muller, Imaging and quantifying chemical and physical properties of native proteins at molecular resolution by force-volume AFM. *Angew. Chem. Int. Ed.* **50**, 12103–12108 (2011).

Acknowledgments: We acknowledge K. Feldman and J. Vermant for access to SLS measurements and for useful discussions. We also thank P. Ashby for constructive feedback and inspiring discussions. **Funding:** J.V. acknowledges funding from the European Union's Horizon 2020 research and innovation programme under the Marie Skłodowska Curie grant agreement 888076. **Author contributions:** Author contributions are defined on the basis of the CRediT (Contributor Roles Taxonomy) and listed alphabetically. Conceptualization: L.I. Formal analysis: J.V. Funding acquisition: L.I. and J.V. Investigation: S.N.R. and J.V. Methodology: L.I., S.N.R., and J.V. Project administration: L.I. Resources: S.N.R. and J.V. Software: S.N.R. and J.V. Supervision: L.I. Validation: S.N.R. Visualization: L.I, S.N.R., and J.V. Writing—original draft: L.I., S.N.R., and J.V. Writing—review and editing: L.I., S.N.R., and J.V. **Competing interests:** The authors declare that they have no competing interests. **Data and materials availability:** All data needed to evaluate the conclusions in the paper are present in the paper and/or the Supplementary Materials.

Submitted 24 March 2022
Accepted 23 September 2022
Published 9 November 2022
10.1126/sciadv.abq2019